11th AIAA/CEAS Aeroacoustics Conference (26th AIAA Aeroacoustics Conference)
23 - 25 May 2005, Monterey, California

AIAA 2005-2960

Three-Dimensional Application of DAMAS Methodology for Aeroacoustic Noise Source Definition

Thomas F. Brooks* and William M. Humphreys, Jr.†
NASA Langley Research Center, Hampton, VA. 23681

At the 2004 AIAA/CEAS Aeroacoustic Conference, a breakthrough in acoustic microphone array technology was reported by the authors. A Deconvolution Approach for the Mapping of Acoustic Sources (DAMAS) was developed which decouples the array design and processing influence from the noise being measured, using a simple and robust algorithm. For several prior airframe noise studies, it was shown to permit an unambiguous and accurate determination of acoustic source position and strength. As a follow-on effort, this paper examines the technique for three-dimensional (3D) applications. First, the beamforming ability for arrays, of different size and design, to focus longitudinally and laterally is examined for a range of source positions and frequency. Advantage is found for larger array designs with higher density microphone distributions towards the center. After defining a 3D grid generalized with respect to the array's beamforming characteristics, DAMAS is employed in simulated and experimental noise test cases. It is found that spatial resolution is much less sharp in the longitudinal direction in front of the array compared to side-to-side lateral resolution. 3D DAMAS becomes useful for sufficiently large arrays at sufficiently high frequency. But, such can be a challenge to computational capabilities, with regard to the required expanse and number of grid points. Also, larger arrays can strain basic physical modeling assumptions that DAMAS and all traditional array methodologies use. An important experimental result is that turbulent shear layers can negatively impact attainable beamforming resolution. Still, the usefulness of 3D DAMAS is demonstrated by the measurement of landing gear noise source distributions in a difficult hard-wall wind tunnel environment.

Nomenclature

a_m	shear layer refraction amplitude correction for e_m
$\hat{A}$	DAMAS matrix with $A_{nn'}$ components
$A_{nn'}$	reciprocal influence of beamforming characteristics between grid points
B_ℓ	longitudinal beamwidth, $R_2 - R_1$
B'_ℓ	forward-defined longitudinal beamwidth, $2(R_0 - R_1)$
B_{Wo}	lateral beamwidth of 3 dB down from beam peak maximum, $= B$ of Ref. 1
c_0	medium speed of sound
CSM	cross spectral matrix
D	diameter of array
DR	diagonal removal of $\hat{G}$ in array processing
$\hat{e}$	steering vector for array to focus location
e_m	component of $\hat{e}$ for microphone m
f	frequency

*Senior Research Scientist, Aeroacoustics Branch, Associate Fellow AIAA.

†Senior Research Scientist, Aeroacoustics Branch, Senior Member AIAA.

Δf	frequency bandwidth resolution of spectra
FFT	Fast Fourier Transform
ϕ	array elevation angle
$G_{mm'}$	cross-spectrum between p_m and $p_{m'}$
$\hat{G}$	matrix (CSM) of cross-spectrum elements $G_{mm'}$
γ	lateral resolution
H	height of chosen scanning plane
i	iteration number
K	acoustic wave number, $2\pi f / c_0$
LADA	Large Aperture Directional Array
λ	longitudinal resolution
m	microphone identity number in array
m_0	total number of microphones in array
n	grid point number on scanning plane(s)
M	wind tunnel test Mach number
MEMS	Micro-Electro-Mechanical System (microphone sensors)
N	total number of grid points over scanning plane(s)
p_m	pressure time records from microphone m
P_m	Fourier Transform of p_m
QFF	Quiet Flow Facility
Q_n	idealized P_m for modeled source at n for quiescent acoustic medium
r	radial position on array face with respect to center
r_c	distance r_m for m being the center c microphone
r_m	retarded coordinate distance to m, $\tau_m c_0$
r_0	radius of array
R	distance of array from scanning plane
R_0	distance of array to source location
R_1	distance of array to 3dB-down array response location forward of source
R_2	distance of array to 3dB-down array response location aft of source
SADA	Small Aperture Directional Array
STD	standard or classical array processing
T	complex transpose (superscript), also block of time data
TE	trailing edge
τ_m	propagation time from grid point to microphone m
W	width of scanning plane
Δx	widthwise spacing of grid points
x, y, z	array coordinates
x_T, y_T, z_T	tunnel coordinates
$\hat{X}$	matrix of X_n terms
X_n	"noise source" at grid point n with levels defined at array, $\mathrm{Q}_n^* \mathrm{Q}_n$
Δy	heightwise spacing of grid points
$Y(\hat{e})$	output power response of the array at focus location
$\hat{Y}$	matrix of Y_n terms
Y_n	$Y(\hat{e})$, when focused at grid point n
Δz	longitudinal spacing of grid points

I. Introduction

Traditional microphone array results represent noise sources that are convolved with array beamform response functions, which depend on array geometry, size, source positions, and frequency. The Deconvolution Approach for the Mapping of Acoustic Sources (DAMAS) method[1] represents a significant technology advance by removing these beamforming characteristics from output presentations. This can render an accurate and explicit definition of source strength and location. The authors in Ref. 1 dealt with DAMAS processing only for single two-dimensional (2D) scanning planes. The current study takes the first step at three-dimensional (3D) DAMAS processing.

One can readily perform 3D processing with DAMAS simply by defining evaluation grid points on other than on a single plane. A primary issue that arises is one of attainable DAMAS resolution, which in turn depends on conventional beamforming resolution. For 2D lateral beamforming where a planar array focuses forward over a plane parallel to the face of the array, it was found[1] that DAMAS can spatially resolve as small as 5 to 20% of a lateral beamwidth (defined by 3 dB down array response). The smaller arrays have little or no focusing ability depth-wise (or longitudinally), so the "longitudinal beamwidth" may not be finite. The larger the array, the higher the ability is to focus depth-wise. However, too large an array would present a measurement dilemma in aeroacoustics, in that the array would enclose differing directivity regions of a source being measured, thus nullifying the measured results (since uniform radiation of any source being measured is assumed over the array traditional processing). In addition to size, array sensor distribution design also affects both lateral as well as longitudinal focusing characteristics.

The present paper makes a first examination of 3D beamforming and corresponding DAMAS source distribution solutions, with regard to array design and size, as well as grid distribution. Classical beamforming is examined with respect to its ability to focus longitudinally and laterally as a function of array design and size with respect to source position and frequency. Three existing experimental designs are examined in some detail. Point source simulations and experimental data using a generalized grid are used to demonstrate attainable 3D resolution for beamforming and DAMAS. Array data obtained during aeroacoustic testing of a flap is used to examine localized and distributed sources. The role of test conditions such as the presence of turbulent shear layer on attainable spatial resolution is observed. Also, examined is a landing gear configuration in a hard wall wind tunnel environment with an array mounted on the sidewall.

II. Basic Beamforming and DAMAS

Figure 1 illustrates a generalized arrangement for a phased array distribution of m_0 microphones located outside a flow field containing an aeroacoustic model. A scanning plane of grid points is defined over the noise source region. Additional planes are shown that may be used when 3D distributions of sources are to be accounted for. The beamforming approach involves the generation of steering vectors associated with each microphone with respect to the chosen steering location.

In Fig. 1, the steering location is designated as grid point n. The steering vector is

$$\hat{e} = \text{col}\begin{bmatrix} e_1 & e_2 & \cdots & e_{m_0} \end{bmatrix} \tag{1}$$

where the component for each microphone m is

$$e_m = a_m \frac{r_m}{r_c} \exp\{j2\pi f \tau_m\} \tag{2}$$

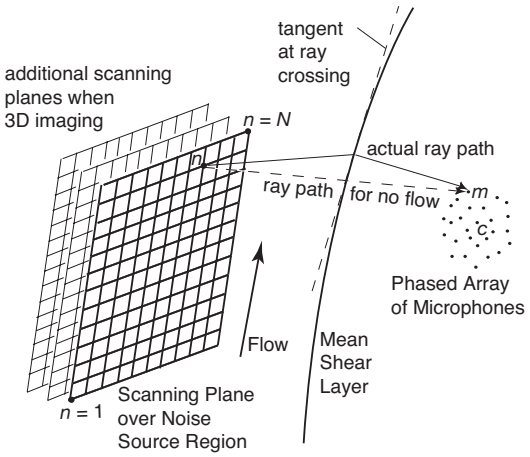

Figure 1. Illustration of open test configuration where the microphone array is placed outside the flow region containing the noise source scanning plane region.

The vector components serve to phase shift each microphone signal to allow constructive summing of contributions from the chosen locations. The steering vector contain terms that account for the mean amplitude a_m and phase changes due to convected and refracted sound transmission through the shear layer to each microphone.

τ_m is the time required to propagate from grid point n to microphone m. In retarded coordinates, r_m is the distance from microphone to the scanning location and r_c is that for the reference center microphone.

The cross-spectrum matrix (CSM) is composed of cross spectra elements and is[1]

$$\hat{G} = \begin{bmatrix} G_{11} & G_{12} & \cdots & G_{1m_0} \\ \vdots & G_{22} & & \vdots \\ \vdots & & \ddots & \vdots \\ G_{m_0 1} & & & G_{m_0 m_0} \end{bmatrix} \tag{3}$$

where each term is the cross-spectrum between each combination of the array microphone using Fast Fourier Transformed (FFT) processed data. For classical or standard (STD) array beamforming, the output power spectrum (or response) of the array is obtained from

$$Y(\hat{e}) = \frac{\hat{e}^T \hat{G} \hat{e}}{m_0^2} \tag{4}$$

Here $Y(\hat{e})$ is a mean-pressure-squared per frequency bandwidth quantity. The division by the total number of array microphones m_0-squared serves to reference levels to that of an equivalent single microphone measurement. Figure 2 illustrates a typical array result presentation over a plane through a source region showing dB level contours of $Y(\hat{e})$. Shading algorithms[1,2,3] in connection with Eq. (4) can be used over distributions of array microphones to modify and control the array beampattern beamwidth B defined as the width across the main response lobe over which the sensing level is within 3 dB from the peak level. Also, to improve dynamic range and remove extraneous noise, the diagonal of the cross-spectral matrix can be removed to obtain a special "Diagonal Removal (DR)" form[1,4] of Eq. (4).

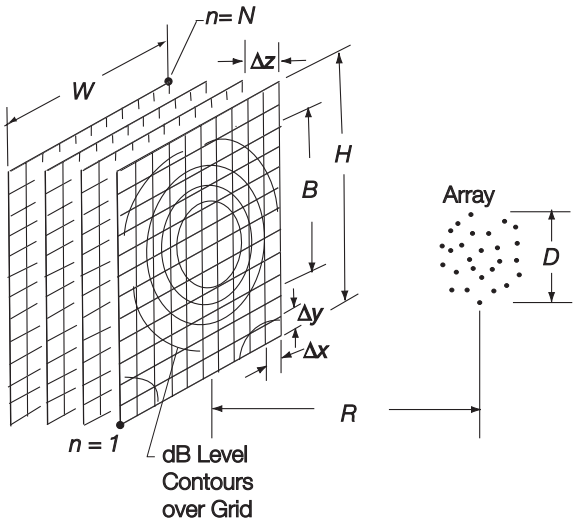

Figure 2. Geometric parameters of the array and source region scanning plane for DAMAS applications.

DAMAS inverse problem definition and solution. As detailed in Ref. 1, the purpose is to pose the array problem such that one can back-out a unique distribution of sources that would fully explain the array output. Defining a pressure transform P_m (for microphone m) to be related to a modeled source located at position n in the source field, one gets

$$P_{m:n} = Q_n e_{m:n}^{-1} \tag{5}$$

where for the modeled source, $X_n \propto Q_n^* Q_n$ is the pressure-squared amplitude of the modeled noise at position n. From this, one obtains the modeled microphone array cross-spectral matrix CSM, $\hat{G}_{n_{\text{mod}}}$, for a single source located at n. Upon summing sources from all n, the total modeled CSM is $\hat{G}_{\text{mod}}$. Then the modeled array output is

$$Y_{n_{\text{mod}}}(\hat{e}) = \left[\frac{\hat{e}^T \hat{G}_{\text{mod}} \hat{e}}{m_0^2} \right]_n \tag{6}$$

By equating $Y_{n_{\text{mod}}}(\hat{e})$ with processed $Y(\hat{e})$ from measured data, we have, when all sources over all n are considered statistical independent,

$$\hat{A}\hat{X} = \hat{Y} \tag{7}$$

with $\hat{A}$ being defined to have the components

$$A_{nn'} = \frac{\hat{e}_n^T [\ ]_{n'} \hat{e}_n}{m_0^2} \tag{8a}$$

where the bracketed term is given by

$$\begin{bmatrix} \left(e_1^{-1}\right)^* e_1^{-1} & \left(e_1^{-1}\right)^* e_2^{-1} & \cdots & \left(e_1^{-1}\right)^* e_{m_o}^{-1} \\ \left(e_2^{-1}\right)^* e_1^{-1} & \left(e_2^{-1}\right)^* e_2^{-1} & & \vdots \\ & & \ddots & \vdots \\ & & & \left(e_{m_o}^{-1}\right)^* e_{m_o}^{-1} \end{bmatrix} \tag{8b}$$

Equation (7) represents a system of linear equations relating a spatial field of point locations, with beamformed array-output responses Y_n, to equivalent source distributions X_n at the same point locations. Reference 1 gives the details of the derivation above as well as the iterative solution method.

2D Application Simulation. Figure 2 shows parameters found to be important in defining requirements for the DAMAS calculations. It was found[1] that a grid step size Δx (or Δy) satisfying

$$0.05 \le \Delta x / B (\text{or } \Delta y / B) \le 0.2 \tag{9}$$

is representative of the resolution range attainable for a physical distribution of sources. Nominally one can denote the resolution as $\gamma \approx 0.15B$. Much finer resolution would give more detail than physically feasible and much coarser resolution would give less detail than needed and perhaps cause aliasing error (in analogy with that of FFT signal processing) in the DAMAS solutions. The spatial extent ratio is required to be at least W/B (and H/B) ≥ 1, because it must be large enough that discrimination is apparent over the grid range in order that the grid points represent independent contributions to the DAMAS solution. With the variation over a distance B of only 3 dB, larger expanses are better.

Figure 3 shows the example[1] of 2D beamforming and DAMAS for an ideal (synthetically generated) point source at R = 60" on a W = H = 50" plane. The array, SADA, is 7.8" in diameter (its design will be detailed subsequently). With $\Delta x = \Delta y$ =1" and beamwidth $B \approx 1$ foot, $\Delta x / B$ = .083. The top left frame of Fig. 3 shows a contour of array response in dB, when the array is focused at different grid locations over the plane, using standard (STD) processing of Eq. (4). DAMAS results are shown for one iteration (i = 1) of the DAMAS solver over the plane, for i=1000 iterations, and for i=5000 iterations. It is seen that progressively better, sharper DAMAS solutions for the point source is attained with more iterations. Sharper results are attainable for somewhat coarser grid spacing Δx.

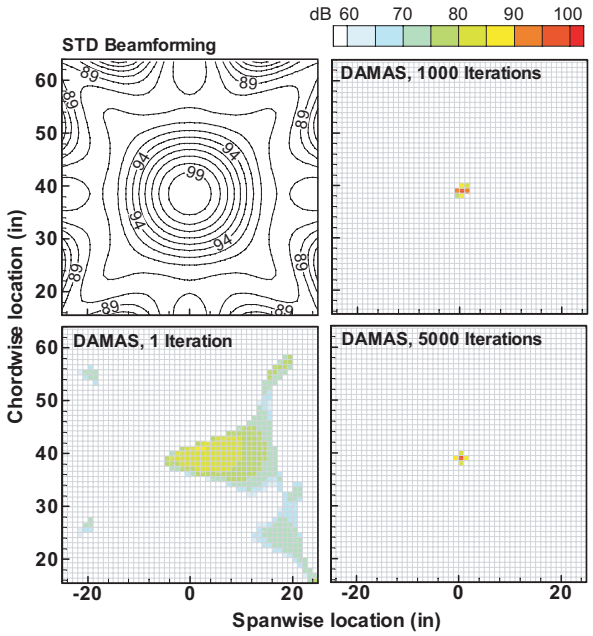

Figure 3. Synthetic point source – SADA STD processing for 50"x50" scanning plane that is 5' away. Resolution Δx =1". Frequency f =10 kHz and $\Delta x / B \approx$0.083.

III. 3D Beamforming

SADA and LADA. The Small Aperture Directional Array (SADA^2) of diameter D = 7.8" and the Large Aperture Directional Array (LADA^2) of diameter D = 34" are used in this section to illustrate 3D beamforming. (Note that the microphone patterns of these two arrays will be given in the following section.) Whereas Fig. 3 shows a lateral cut through a source at a distance R_0 = 60" from the center of and perpendicular to the face of the SADA, Fig. 4 shows a longitudinal cut passing through both the source and the SADA center. The levels are referenced to zero dB response when the array is focused to the point source. The 3 dB-down locations in front of the source toward the array, designated as R_1, and 3 dB-down to the sides of the source, whose distance between is B_{Wo}, are reference measures of the beam pattern. In Fig 2 and previous discussions, the lateral B_{Wo} is referred to as simply B. With the SADA, the large ratio of R_0/D (=7.7) renders broad (large B_{Wo}) and elongated beam patterns, which do not "close" (i.e., do not form a closed beampattern) except at very large z distances (not shown in this scale) for the highest frequencies. In Fig. 5, corresponding results for the LADA (where R_0/D =1.77) are shown. For all frequencies, the beam pattern is more tightly "focused", with R_1 being closer to R_0 and the pattern less elongated. At 6 kHz, the pattern is seen tighten, compared to that at 1 kHz. It is seen to "close", or drop in level, at z values beyond the source location. There the 3 dB-down location is designated by R_2. At higher frequencies of 10 and 40 kHz, the beam patterns are seen to tighten considerably (note the change of scales). Tables 1 and 2, to be subsequently discussed, include values for these reference length measures.

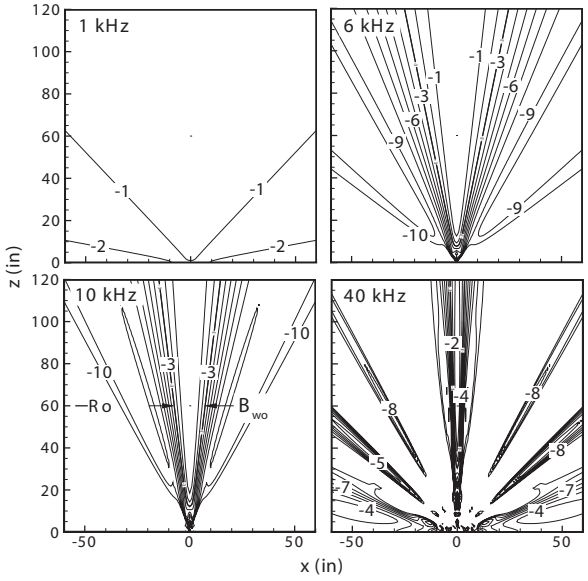

Figure 4. SADA beamforming along a longitudinal plane with point source at R_0=60" (for f =1, 6, 10 and 40 kHz).

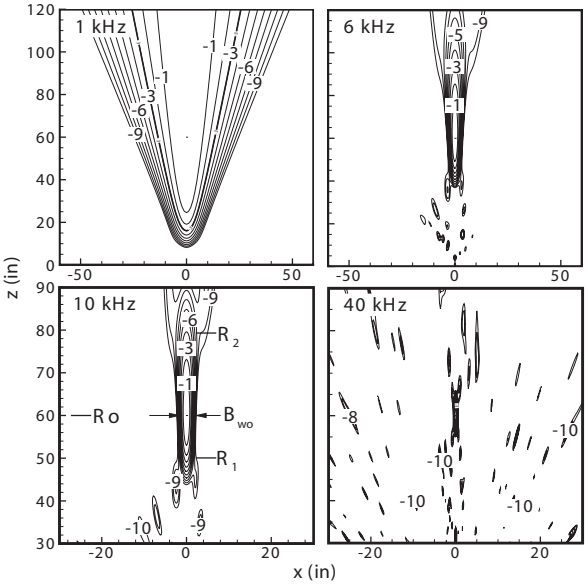

Figure 5. LADA beamforming along a longitudinal plane with point source at R_0=60" (for f =1, 6, 10 and 40 kHz).

Beamwidth Parameters and Array Configurations. A sketch of a beam pattern defined by the 3 dB-down response curve is given in Fig. 6 for an array of diameter D, showing the lateral beamwidth B_{Wo} at R_0 and locations R_1 and R_2. A longitudinal beamwidth is defined as

$$B_l = R_2 - R_1 \tag{10}$$

and, also, an alternate definition is the "forward-defined" longitudinal beamwidth B_l',

$$B_l' = 2(R_0 - R_1) \tag{11}$$

The following analysis determines relations for these beamwidths as function of array type and source distance. This analysis is facilitated by viewing the array as a circular disk with a continuous sensing surface. This also permits an examination of array weighting (or microphone density) sensitivity with regard to an array's ability to focus in 3D.

For the circular array "disk" in Fig. 6, the Fourier transform $F=F(f)$ of the resultant acoustic load response is related to the integral of the Fourier transform $P(f,r,\theta)$ of the acoustic pressure at radius r and polar angle θ over the disk,

$$F = \iint W(r,\theta)P(f,r,\theta)E(r,\theta)rdrd\theta \tag{12}$$

where $W(r,\theta)$ is an array "sensitivity" weighting and $E(f,r,\theta)$ is an "array steering" term. $W(r,\theta)$ can be used to define a microphone density over the disk. $E(f,r,\theta)$ can be used to focus array response to specific locations in the sound field. The array disk response in terms of dB is

$$dB = 10Log(F^*F) \tag{13}$$

The term F^*F replaces $Y(\hat{e})$ of Eq. (4) for the present continuous disk "array". Equations (12) and (13) were evaluated for a number of array design weightings $W(r)$ (microphone density variations) to determine the likelihood of the existence of optimum configurations for longitudinal focusing. The evaluations were carried out numerically using a mathematical software package and, alternately, using dense sensor distributions with standard array programming.

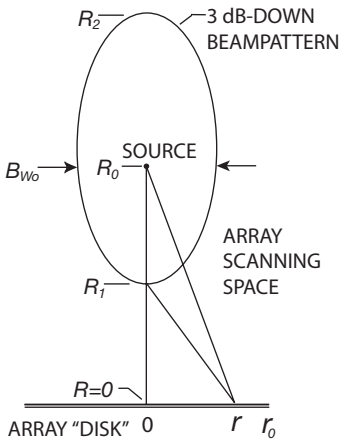

Figure 6. Sketch of a 3 dB-down beam pattern over a longitudinal plane for a point source at R_0

Figure 7 shows sketches of these array disk weightings considered along with the LADA, SADA, and MEMS array (to be discussed). The Uniform distribution, for equal sensitivity across the array, is contrasted with the Conical distribution (in proportion to r/r_0) with zero sensitivity at the disk center $r = 0$ and the greatest sensitivity at the edge at $r = r_0$, the Inverse Conical $(1-r/r_0)$, as well as the inverse weightings $(r/r_0)^{-1}$ and $(r/r_0)^{-3/2}$ with sensitivities greatest approaching the center $r = 0$. In Fig. 8, array responses are shown, as represented by the 3 dB-down contours from the peak level at R_0 for the array designs. All diameters D were set to that of the LADA for comparison purposes, $R_0 = 5$', and $f = 10$ kHz. In Fig. 8 (a) which shows the curves to the correct relative scale, it is seen that for all designs, the longitudinal beamwidths B_l are large compared to their lateral beamwidths B_{Wo}. This is disappointing to the extent it would be desirable to attain good and near-equal resolution of noise sources in all directions. Still there are important differences between the resolutions of the different designs, which may make 3D focusing practical or not depending on application. Differences are more easily seen in Fig. 8 (b) where the lateral coordinate is stretched. The array legends are listed in order of the ratio B_l / B_{Wo} that should be an indicator of how well the 3D focusing is for this f, D, and R_0 case. The finite sensor number array designs do well in this comparison. The SADA has a relatively good B_l / B_{Wo} of 7.8. This is followed by the $(r/r_0)^{-1}$, $(r/r_0)^{-3/2}$, LADA, MEMS, Uniform, Conical, and Inverse Conical designs.

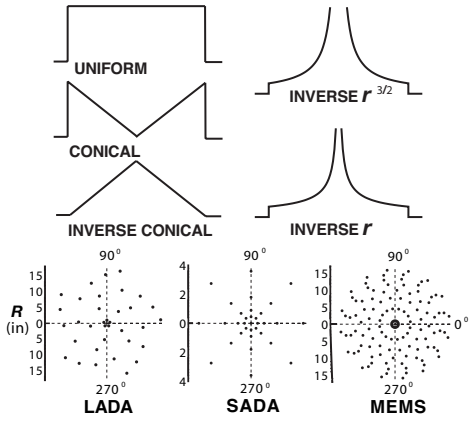

Figure 7. Array weighting distribution functions considered over face of circular arrays.

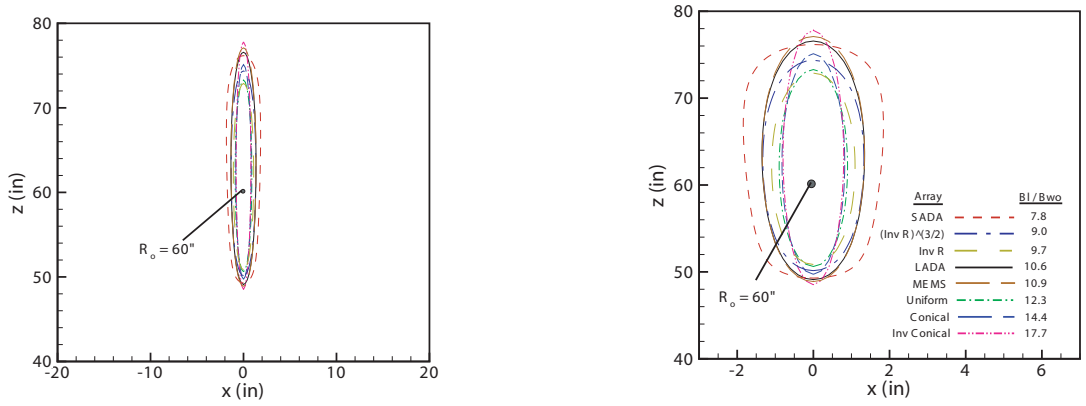

a. to SADA **b. expanded scale**

Figure 8. Beam patterns of array response for arrays with differing weighting distributions (all are evaluated for R_0/D = 1.765).

Table 1 quantifies the lateral and longitudinal beamwidth values for the same array designs of Figs. 7 and 8, except SADA and the MEMS array are listed using their own diameters D. The values for SADA outer cluster, appropriate for the blended results presented in Ref. 1 at 10 kHz, are additionally presented. In Table 1, the lateral beamwidth B_{Wo} is defined from the numerical calculations and the constant C_0 is subsequently defined using

$$B_{W_0} = \frac{C_0 R_0}{KD} \tag{14}$$

Table 1. 3D Beamforming parameters for specific array designs for source at R_0 = 5' and f = 10 kHz

Array Disk Weighting	D (ft.)	R_1 (ft.)	R_2 (ft.)	B_l (ft.)	B_l' (ft.)	$-C_1$	B_{wo} (ft.)	C_0	B_l/B_{wo}	B_l'/B_{wo}
UNIFORM	2.83	4.23	6.05	1.82	1.54	1.87	0.15	4.71	12.3	10.4
CONICAL	2.83	4.18	6.20	2.02	1.64	2.08	0.14	4.45	14.4	11.7
INVERSE CONICAL	2.83	4.10	6.40	2.30	1.80	2.33	0.13	4.10	17.7	13.8
INVERSE r/ro	2.83	4.26	6.00	1.74	1.48	1.80	0.18	5.70	9.7	8.2
INVERSE $(r/ro)^{3/2}$	2.83	4.20	6.18	1.98	1.60	2.05	0.22	6.90	9.0	7.3
LADA - Unweighted	2.83	4.09	6.38	2.29	1.82	2.33	0.22	6.90	10.6	8.4
SADA - Unweighted	0.65	1.01	∞	∞	7.98	2.30	1.23	8.98	∞	6.5
SADA - Outer Cluster	0.65	1.04	∞	∞	7.92	2.30	0.86	6.28	∞	9.2
MEMS - Unweighted	2.46	3.78	6.91	3.13	2.44	2.57	0.24	6.73	13.0	10.2

Parameter Evaluation. The influence of array size, frequency, and source distance with respect to longitudinal beamforming are now examined. Referring to Fig. 6, for a point source at a distance R_0, the pressure perceived over the face of the disk is $P = P_0 \exp(i\varphi_0)$, where the phase at radius r is $\varphi_0 = K(\sqrt{R_0^2 + r^2} - R_0)$ with respect to that at the disk center where $r = 0$. This analysis assumes R_0 to be sufficiently larger than r to allow magnitude P_0 to be simply taken as uniform over the array. Specializing to the case of focusing the array to a point at distance R along the line through the array center and the source (thereby making the problem independent of θ), one can set, in Eq. (12), $E = \exp(i\varphi)$, where $\varphi = K(\sqrt{R^2 + r^2} - R)$. The phase response over the disk at radius r is then

$$\varphi_0 - \varphi = K(\sqrt{R_0^2 + r^2} - R_0) - K(\sqrt{R^2 + r^2} - R) \tag{15}$$

At $R = R_0$, the phase would be zero over the whole array disk for maximum response for focusing at the source. It is hypothesized that in order for an array, focusing at R, to have a response (through Eq. (12)) that is a "set portion" of the maximum response, the phase $\varphi_0 - \varphi$ at any specific r would have a "set value", which is dependent on the weighting $W(r)$. Defining this "set portion" of response to be 3 dB down, and taking the specific r to be $r_0 = D/2$, and $R = R_1$ one has

$$C_1 = K(\sqrt{R_0^2 + r_0^2} - R_0) - K(\sqrt{R_1^2 + r_0^2} - R_1) \tag{16}$$

Equation (16) can be rearranged to give

$$R_1 = \frac{D}{4}\{[] - []^{-1}\} \tag{17}$$

where the bracketed term [] is

$$[] = \left[\frac{2C_1}{KD} - \sqrt{\left(\frac{2R_0}{D}\right)^2 + 1} + \frac{2R_0}{D} \right] \tag{18}$$

A corresponding term for $R = R_2$ is C_2 where C_2 is defined the same as C_1 of Eqs. (16)-(18), but with subscript 2 replacing 1 in both R_1 and C_1. Note that $C_2 = -C_1$. This relationship and the fact that the constants are virtually independent of frequency, array diameter, and R_0, at sufficiently large R_0/D, were verified in numerical calculations. Values of C_1 are given in Table 1 for each array design.

As in Fig. 8, Table 1 considers only $f = 10$ kHz, although results for other frequencies can be determined from the above combination of equations. For the LADA and SADA, Figs. (9) and (10) show values of B_l, B_l', B_{Wo}, B_l/B_{Wo}, and B_l'/B_{Wo} as functions of frequency f.

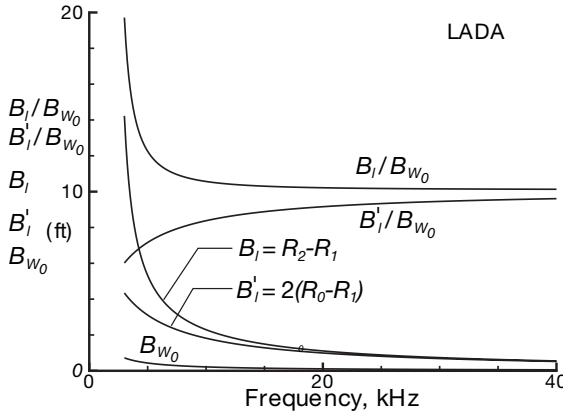

Figure 9. LADA lateral and longitudinal beamwidth parameters with respect to frequency. For R_0/D = 1.765 of Fig. 4.

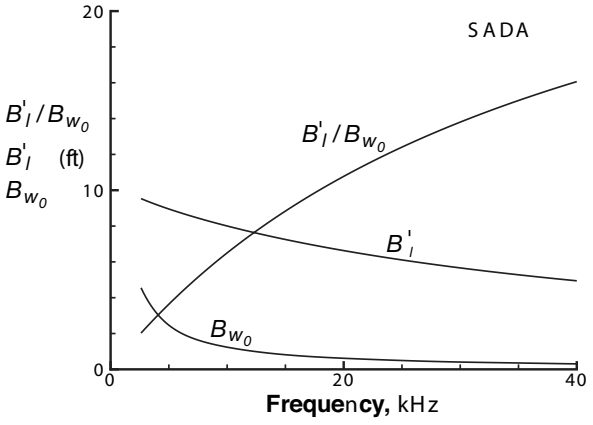

Figure 10. SADA lateral and longitudinal beamwidth parameters with respect to frequency. For R_0/D = 7.69 of Fig. 5.

It is seen that the 10 kHz cases of Fig. (8) and Table 1 show only intermediate relationships for the parameters that stabilize at the highest frequencies. For the LADA in Fig. (9), B_l' is seen to approach a value somewhat less than B_l. For the SADA, B_l is off-scale. Figure (11) shows both B_l/B_{Wo} and B_l'/B_{Wo} as a function of R_0/D, for a number of KD values for the LADA sensor design. A corresponding figure for the SADA sensor design would be similar. The figure shows that B_l and B_l' approach a set ratio with one another for high frequencies independent of the source distance from the array.

It is seen that array design does affect 3D focusing characteristics as illustrated by Fig. 8. However, there is no obvious array sensor design that would allow very high-resolution 3D focusing (small values of B_l/B_{Wo}) at practical values of R_0/D. In Fig. 11, the values of R_0/D are indicated for the LADA and the SADA in the QFF. This range is believed to represent a practical R_0/D range in aeroacoustic testing, although for some applications, LADA is regarded as too large[4].

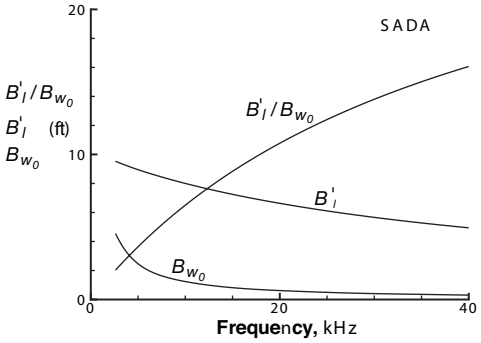

Figure 11. Ratio of beamwidth parameters with respect to R_0/D for array KD values. Array microphone configuration is that of the LADA.

IV. 3D Beamforming and DAMAS applications

Grid definition and Simulations: Simulations for the LADA and SADA are performed to determine the degree to which 3D spatial source distributions can be resolved using DAMAS. Results are shown in Figs. 12-15.

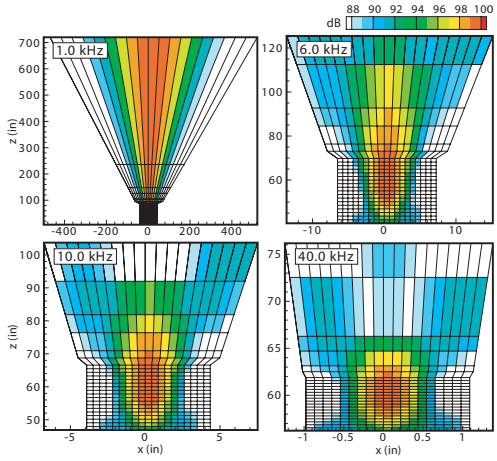

Figure 12. LADA longitudinal plane of 3D Beamforming output for synthetic point source at R_0 = 60", for 1, 6, 10, and 40 kHz. Grid adapted to beamform parameters.

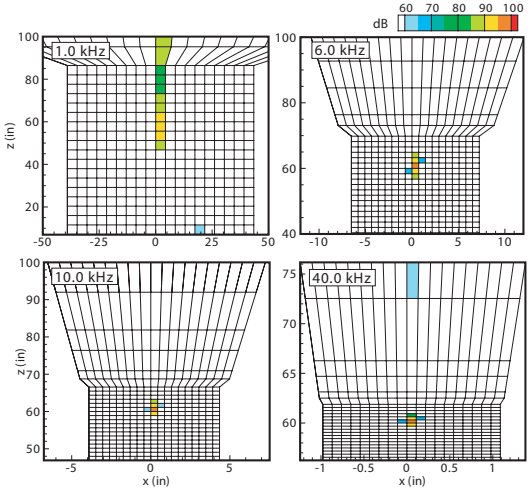

Figure 13. LADA 3D DAMAS solutions for cases of Fig. 12. Reduced ranges of z grid are shown.

The grid patterns are adapted to beamform parameters that are calculated by the preceding equations. The philosophy of the adapted grid pattern is consistent with that used in 2D applications[1] to meet the hypothesized needs for efficient DAMAS solutions. The grid spacing used is $\Delta x / B_{Wo} = \Delta y / B_{Wo} = .167$. For reference, the approximate lateral resolution is taken as this spacing, $\gamma \approx \Delta x = .167\, B_{Wo}$ which is consistent with that range given by Eq. (9). Because the resolution attainable in the longitudinal direction is the subject of study here, the ratio $\Delta z / B_l'$ was kept to a small .05 value in the vicinity of the source in order to be able to observe the resolution character. The width of the lower rectangular grid stack is kept at $C_{\mathrm{Wo}}B_{\mathrm{Wo}}$, where C_{Wo} is the number of lateral beamwidths that are chosen to enclose the source region containing R_0. For the figures, C_{Wo}=3.5 is used. In this stack of 19 grid planes, the first plane starts at z=R=R_0–

1.2(R_0-R_1), others have Δz=0.1(R_0-R_1) spacing, and the last ends at R=R_0+0.6(R_0-R_1). Above the rectangular stack, the six expanding-width grid planes have widths equal to $C_{Wo}B_W$, where B_W is defined by Eq. (14) except R replaces R_0. The positions for these grids are: first, R = R_0+0.8(R_0-R_1); second, R_0+ (R_0-R_1); third, R_0+1.5(R_0-R_1); forth, R_0+2(R_0-R_1); fifth, R_0+4(R_0-R_1); and last, 1.2R_2. However, if R_0+ 2(R_0-R_1)≥ R_2, the second, third, and forth positions become, R_0+ .4(R_0-R_1)+.4(R_2- R_0), .5[R_2+ R_0+ .4(R_0-R_1)+.4(R_2- R_0)], and R_2, respectively. Also, if R_0+ 4(R_0-R_1)≥ R_2, the fifth becomes 1.1 R_2. Finally, the last grid plane position becomes 10R_0, if R_2≥10R_0.

For the LADA, Fig. 12 shows a horizontal (longitudinal) plane cut of 3D beamforming levels for frequencies at 1, 6, 10, and 40 kHz. Figure 13 shows the same for the corresponding DAMAS levels except the z scale is limited to 100 inches and below in order to show details in the source region. For each frequency, the test grid pattern is square in x and y coordinates, so a vertical plane cut would give the same appearance. The levels are not contour plotted, but are represented by color for each block (the pertinent grid point for the block is located at the bottom left corner). The total number of DAMAS iterations employed over the 11025 grid points was i = 5000. More source dispersion was noted when i = 1000 iterations were used. With the exception of the 1 kHz results, DAMAS successfully recovers the source region near R_0=60". The peak at z = R_0 (where level is about 96.4 dB) and the adjoining grid points account for virtually all the noise source strength. Upon defining the resolution λ as containing all but about 1 dB of the 100 dB source strength, it is seen that $\lambda / B_l^{'} \approx 0.15$ (3 grid points) for frequencies of 6 kHz and above. For 1 kHz, substantial error occurs in the location and energy spread. In Table 2, the resolution results are summarized for these and several other frequencies. For LADA with R_0=60", it is seen that $\lambda / B_l^{'}$ remains at about 0.15. The ratio of longitudinal to lateral resolution λ / γ is in the range of 7 to 8. In the table, the asterisk (*) indicates the entry is only suggestive or that there is no correct answer. This is seen to be the case for lower frequencies where $B_l / B_l^{'} >> 1$, where the longitudinal beamwidth "ceases to close".

For the SADA, the beamform levels and DAMAS results are presented in Figs. 14 and 15. The grid pattern is defined using the same grid generation logic. Figure 15 limits the presented z scale to 200 inches. Except for the highest frequency, the source is not captured. Even then, the energy is substantially spread. The results are summarized in Table 2, where the results are consistent with the LADA results with respect to the condition $B_l / B_l^{'} >> 1$, where there is failure of DAMAS to capture the source.

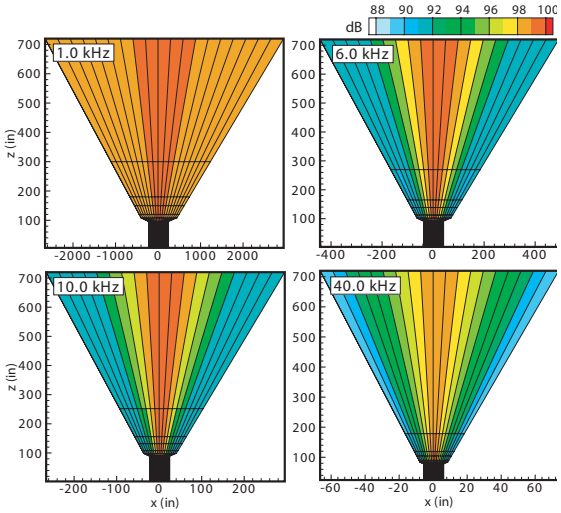

Figure 14. SADA longitudinal plane of 3D Beamforming output. Otherwise key as per Fig. 12.

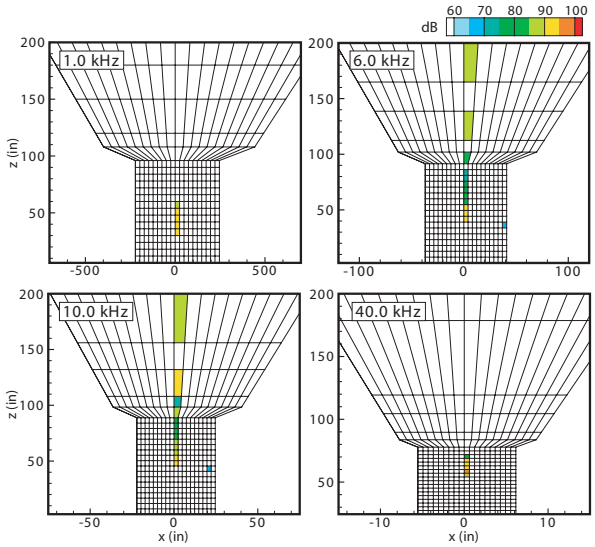

Figure 15. SADA 3D DAMAS solutions for cases of Fig. 14. Reduced ranges of z grid are shown.

Table 2. 3D Beamforming and DAMAS point source simulation resolution results for the LADA and the SADA. R_0=60".

Array	Freq. (kHz)	R_1 (ft.)	R_2 (ft.)	B_l (in.)	B_l' (in.)	B_l/B_l'	B_{wo} (in.)	Δz (in.)	λ (in.)	$\lambda/B_{l'}$	$\Delta x/B_{wo}$	Δx (in.)	λ/γ
LADA	1	1.33	∞	∞	88.0	∞	26.0	4.40	35.2*	0.40*	0.167	4.3	8.1*
	3	2.83	17.16	172.0	52.2	3.3	8.7	2.61	10.4	0.20	0.167	1.5	7.2
	6	3.64	7.80	49.9	32.7	1.5	4.3	1.63	4.9	0.15	0.167	0.7	6.8
	10	4.09	6.38	27.5	21.8	1.3	2.6	1.09	3.3	0.15	0.167	0.4	7.5
	20	4.50	5.61	13.3	11.9	1.1	1.3	0.60	1.8	0.15	0.167	0.2	8.2
	40	4.74	5.29	6.6	6.3	1.1	0.7	0.31	0.9	0.15	0.167	0.1	8.6
SADA	1	*	∞	∞	*	∞	147.7	6.10	*	*	0.167	24.6	*
	3	0.29	∞	∞	113.2	∞	49.2	5.66	*	*	0.167	8.2	*
	6	0.63	∞	∞	104.9	∞	24.6	5.24	*	*	0.167	4.1	*
	10	1.00	∞	∞	96.0	∞	14.8	4.80	33.6*	0.55*	0.167	2.5	21.5*
	20	1.69	∞	∞	79.6	∞	7.4	3.98	23.9*	0.35*	0.167	1.2	22.6*
	40	2.53	175.	2070.	59.3	35	3.7	2.97	14.8*	0.25*	0.167	0.6	24.1*

Experimental Cases

In this section, experimental data are used to validate the resolution results from the simulations and to apply 3D beamforming and DAMAS for several wind tunnel aeroacoustic test setups. Data used are from LADA measurements for a calibration "point source" and from a flap/airfoil model test conducted in the Quiet Flow Facility (QFF) at NASA LaRC. Also used are data acquired with the NASA LaRC MEMS sensor array during landing gear testing in the Virginia Tech (VT) Stability Wind Tunnel. For these cases, unlike the pure tone simulation cases, the results are presented in terms of one-third octave levels. This requires consideration of bandwidth error issues.

Spectral bandwidth. For the array testing[1] done in the QFF, the data has been processed by Fast Fourier Transform (FFT) methods rendering a frequency resolution of Δf = 17.44 Hz = 1/T, where T is the individual data ensemble block size, in units of seconds. For the VT test data, the Δf used was 24.4 Hz. For each cross-spectral component of the CSM, Eq. (3), there is a center frequency and phase associated with each Δf band. With Δf being sufficiently small, there is no error issue with the fact that $\Delta f \neq 0$. But with Δf being small, repeated applications of DAMAS at each Δf are required, and then summed, to produce single one-third octave DAMAS source maps. This is computationally time consuming, so it is desired to increase the bandwidths Δf so that less summations are required to form one-third octave results. The question arises of the error associated with the chosen sizes of Δf and how the bands are formed.

Considered here are cross-spectral errors associated with time delay differences between microphones. First, there is a negative error due to processing when there is a time delay τ between microphones m_k and m_l. The delay τ is dependent on source location, the relative microphone locations, the test median speed-of-sound, and any required shear layer corrections. The FFT processing produces an "estimated" cross spectrum[5]

$$(G_{m_k m_l})_{est} = [1 - \frac{\tau}{T}] G_{m_k m_l} \tag{19}$$

where $G_{m_k m_l}$ is the "actual" cross spectrum. The error is independent of frequency. The error is highest between extreme microphones of the array when focusing to edges of extended scanning planes. The effect is to effectively attenuate the contributions of the outer edges of the array – in contrast to the full coherence that is assumed in matrix $\hat{A}$ of Eq. (7). Equation (19) can be used to guide one's choice of reprocessing with different T block sizes in order to maximize Δf, and still keep error within chosen bounds. To keep the error below 0.2 dB (a stringent choice) in

any of the CSM components, one can reprocess to attain $\Delta f \approx 220$ Hz for the SADA setup geometry in the QFF with a scanning plan at R_o = 60" and 50" wide. For the LADA, $\Delta f \approx 50$ Hz for the same scanning plane and $\Delta f \approx 100$ Hz for a one half size scanning plane (more practical anyway for the LADA in terms of number of required grid points, considering Δx requirements with respect to LADA's smaller B_{Wo} values).

An alternative to reprocessing the cross spectra from the original time signals in order to increase Δf is to combine existing Δf bands vectorially. There is a bias error inherent in doing this, due to variation in phase because of the same time delay τ considered above. An "estimated" cross spectrum with new Δf created by summing bands, would be

$$(G_{m_k m_l})_{est} \approx \frac{1}{\Delta f}\int_{f_1}^{f_2} G_{m_k m_l}\, df \approx \left[\frac{\sin(\pi \Delta f \tau)}{\pi \Delta f \tau}\right] G_{m_k m_l} = \left[\frac{\sin(\pi \tau / T)}{\pi \tau / T}\right] G_{m_k m_l} \qquad (20)$$

where the form for the cross spectrum is taken as $G_{m_k m_l} = \left|G_{m_k m_l}\right| \exp(i 2\pi f \tau)$. Here, $\Delta f = f_2 - f_1$ and T is the block size it would have taken to obtain Δf in normal processing. The bracketed term of Eq. (20) is substantially closer to the value 1 than that of Eq. (19) at small τ / T. For the same level of CSM error, the corresponding Δf values possible for the SADA and the LADA with Eq. (20), are now 3.4 times larger now at $\Delta f \approx$ 750, 170, and 340 Hz compared to the $\Delta f \approx$ 220, 50, and 100 Hz, respectively, given in the last paragraph for Eq. (19).

In the following applications for the QFF and VT tests, Δf were increased by summing bands in accordance with Eq. (20), although a more conservative approach was actually taken by using only about a half of the Δf permitted as guided by the examples given above. In a separate matter, it should be noted that the permissible Δf values, found using Eqs. (19) and (20), are independent of frequency *f*. One could use other criterion for analysis bandwidths Δf such as those for 1/12th octave bands ($\Delta f \approx .058 f_C$) as long as permissible chosen values of Δf are not exceeded at each DAMAS calculation.

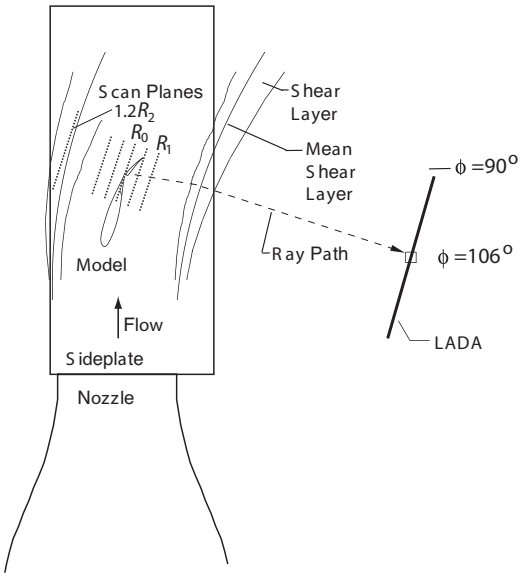

a. Noise path from flap edge to the LADA. Scan planes are for flap noise study.

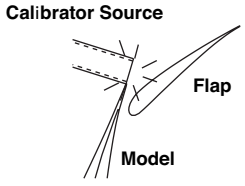

b. Open end of calibration source positioned next to flap edge.

Figure 16. LADA test set-up in QFF for flap noise test and calibration.

QFF "Point" Source Test. A sketch of the LADA positioned outside of the flow field in the QFF is shown in Fig. 16 (a) for the model flap and main airfoil element test set-up. The scan planes shown are for the subsequent study of flap edge and flap cove noise. The airfoil is at 16° angle-of-attack to the vertical. A similar experimental set-up using the SADA was reported in Ref. 1. The LADA is positioned at an angle of ϕ = 106°, referenced to the vertical line through the main element trailing edge (TE) and at a distance of R_0 = 5 feet. The use of the LADA is detailed in Refs. 2. Its microphone arrangement is shown in Fig. 7. Figure 16 (b) shows the calibrator source arrangement located at the TE next to the flap edge. The source is an open end of a one-inch diameter tube emitting broadband noise.

Figures 17 and 18 show, respectively, the 3D beamforming and DAMAS for the calibrator source output with no tunnel flow (i.e., M = 0) and for the same grid pattern as the simulation of Figs. 12 and 13. As mentioned, the presentations are for one-third octave frequency bands, obtained by combining CSM results from a number of

individual 17. 44 Hz bands to obtain Δf =122 Hz, used for evaluations of DAMAS. The DAMAS results were then summed to obtain the one-third octave results. The experimental results displayed in Figs. 17 and 18 show there is an approximate 0.3" off-set in the assumed source center position and some broadening (about 0.4") due to the finiteness (1" diameter) of the source. But there is also some additional longitudinal smearing of about 0.05 to 0.1B_l (1 to 2 blocks) over that found for the synthetic point source results displayed in Figs. 12 and 13. The longitudinal resolution found here is about 6", 5", and 1" for 6, 10, and 40 kHz, respectively.

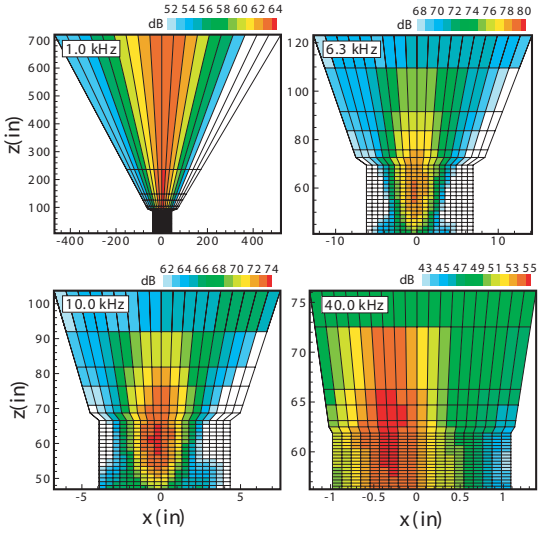

Figure 17. LADA 3D beamforming output for experimental calibration source of Fig. 16 (b) presented over same grid and format of Fig. 12.

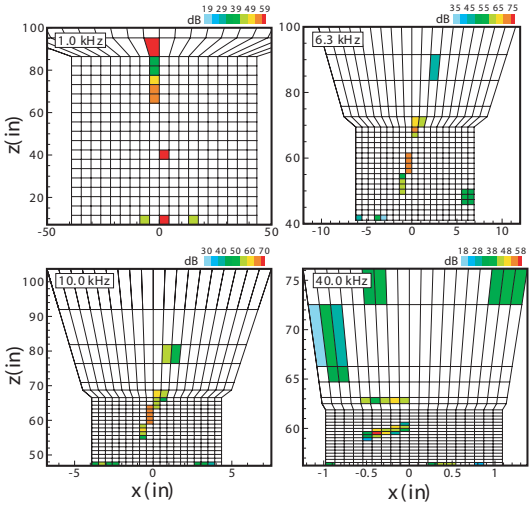

Figure 18. LADA 3D DAMAS results corresponding to Fig. 17

QFF Flap Test. The flap edge test configuration for the LADA in the QFF is shown in Fig. 16 (a). The test case considered is for a 29° flap angle setting and M = 0.11. For a similar test case (see Ref. 1) in which the SADA was used, it was shown there was strong localized flap edge noise and distributed flap cove noise. This case is used here for a 3D DAMAS evaluation for multiple sources of different distributions. Of course, it is already known that both sources can be regarded as being located along one scanning plane that is aligned with the airfoil main element chordline. This scanning plane is designated in Fig. 16 (a) by R_0 (= 60"). For this scanning plane, Fig. 19 shows 2D beamforming contours and DAMAS results over the flap region using $\Delta x = \Delta y = 0.25$" for the LADA with $f_{1/3}$ = 20 kHz ($\Delta x / B_{Wo} = .19$). For this M ≠ 0 tunnel case, Fig. 19 shows results using Diagonal Removal (DR) processing for the first time in this report. The region of the contour plane that is presented as blank actually contains negative pressure-squared beamforming output from the DR processing. DR DAMAS processing was shown in Ref. 1 to give less noisy results by reducing the contributions of extraneous microphone wind self noise from the calculations. (Still, this result shows substantial extraneous "noise" over the scanning plane. This is the result of the array peering through the shear layer turbulence[4], not microphone self noise. This "noise" is more severe for larger arrays. Note that if only 2D results were needed for this measurement exercise then the SADA or a sub-array of the LADA would be preferred.) The strong localized source region at the flap edge and the distributed source along the flap and main airfoil element cove are captured by 2D DAMAS. The total flap edge noise and flap cove noise levels are 44.5 and 42.1 dB, respectively, (These were found for the flap edge by summing over x_T = 39" to 44" and y_T = ± 1" and for the cove by summing over x_T = 38" to 41" and y_T = 1" to 18".) Note that by using LADA sub-arrays of various sizes, DAMAS determines the same total flap edge and flap cove noise levels over the same areas within 1 dB. For the flap edge noise, the above agrees with the 44.6 dB found for the SADA in Ref. 1 for the similar test case mentioned.

In order to perform 3D calculations, a target limit of 20,000 grid points was used, which required a reduction of the scanning plane size from that of Fig. 19 and a reduction of the number of planes compared to Figs. 17 and 18. Figure 16 (a) shows the scanning planes at R = 54" (=R_1), 57", 60" (=R_0), 63", 66", and the last plane at 81" (=1.2 R_2), which partially follow the grid pattern logic previously used. The planes are normal to a line connecting the array center to the trailing edge (TE) and flap edge junction. In the array coordinate y direction shown, the grid used C_{Wo}=3.5. The grid is shown for the array coordinate y (=y_T) spanwise dimension. Figure 20 shows beamforming results over the six scanning planes. The result for the R_0 plane is the same as that of Fig. 19. Although the levels are the highest at R_0, the levels on planes on either side are very close to these. Any de-focusing away from R_0 is barely apparent visually, until the last plane at1.2 R_2. The 3D DAMAS results of Fig. 21, show a somewhat stronger distinction between the scanning planes, although clearly the sources are not isolated to the R_0 plane. (Ideally, the test model sources in the R_0 plane would match those of Fig. 19 and not be included in the other planes.) The noise levels, summed in a manner consistent with that done for Fig. 19 and for the planes with increasing R values are 30.4, 37.8, 42.0, 24.5, 32.0, and 24.2 dB for the flap edge, and 34.5, 34.6, 37.6, 34.2, 34.2, and 29.0 dB for the flap cove. Compare these to the 2D totals of 44.5 and 42.1 dB for the flap edge and flap cove, respectively.

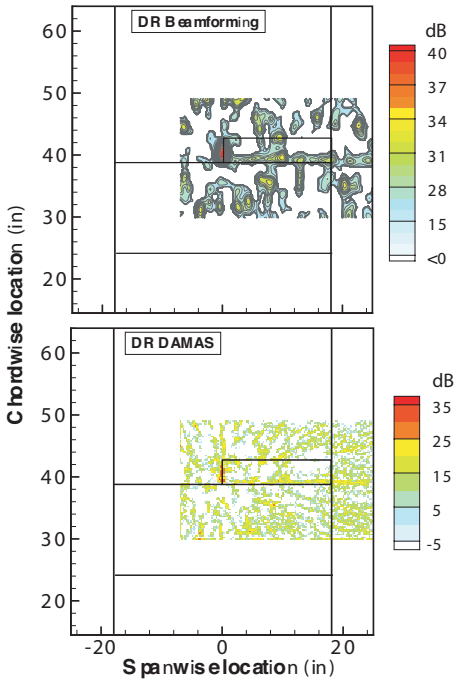

Figure 19. 2D beamforming output and DAMAS for flap noise test. DR processing with $f_{1/3} = 20kHz$ for $\Delta x = 0.25$".

The results are good in that the highest levels are located on the R_0 plane. However, the results are problematic and important in that they indicate that the resolution scale λ is larger than anticipated from the preceding simulations and calibrations. This can directly impact the usefulness of 3D measurements, at least for this test set-up. With the definition that λ is the longitudinal scale that accounts for all but about 1 dB of source level (assumed to be found by the 2D results), one can find λ by combining the pressure-squared values of the R_0 and adjacent planes. For the localized flap edge noise source, one obtains $\lambda \approx 0.25B_l$, but for the distributed flap cove noise source, $\lambda \approx 0.4B_l$. Here B_l is calculated by the forgoing equations. The loss of resolution from $\lambda \approx 0.15B_l$ is viewed by the authors as due to an effective increase in beamwidth B_l due to the presence of the open-jet turbulent shearlayer. As was observed for Fig. 20, the beamformed pattern for the five adjacent planes are very similar with one another with little de-focusing apparent as one moves away from R_0. More difference should be seen across the one beamwidth distance, B_l, that is spanned by the five planes. It is not an issue with DAMAS per se – but with beamforming. As discussed to some length in Ref. 4, sound produced by the model is transmitted through the turbulent shear layer on its way to the microphones. The ray paths are scattered by turbulence with respect to the mean refracted ray paths, thereby randomizing the noise received by each microphone. The importance of this scatter is more severe for the larger array sizes, because different microphones receive rays of different scatter paths thereby reducing coherence over the face of the array. This serves to spatially blur the source. This has not been considered a general problem for lateral beamforming for large arrays where resolution is already high. And no energy is lost in spatial integration[4] if one can increase spatial expanse. However, for longitudinal beamforming, resolution blurring is an issue if intrinsic beamwidth is already considered too large to define the source field properly.

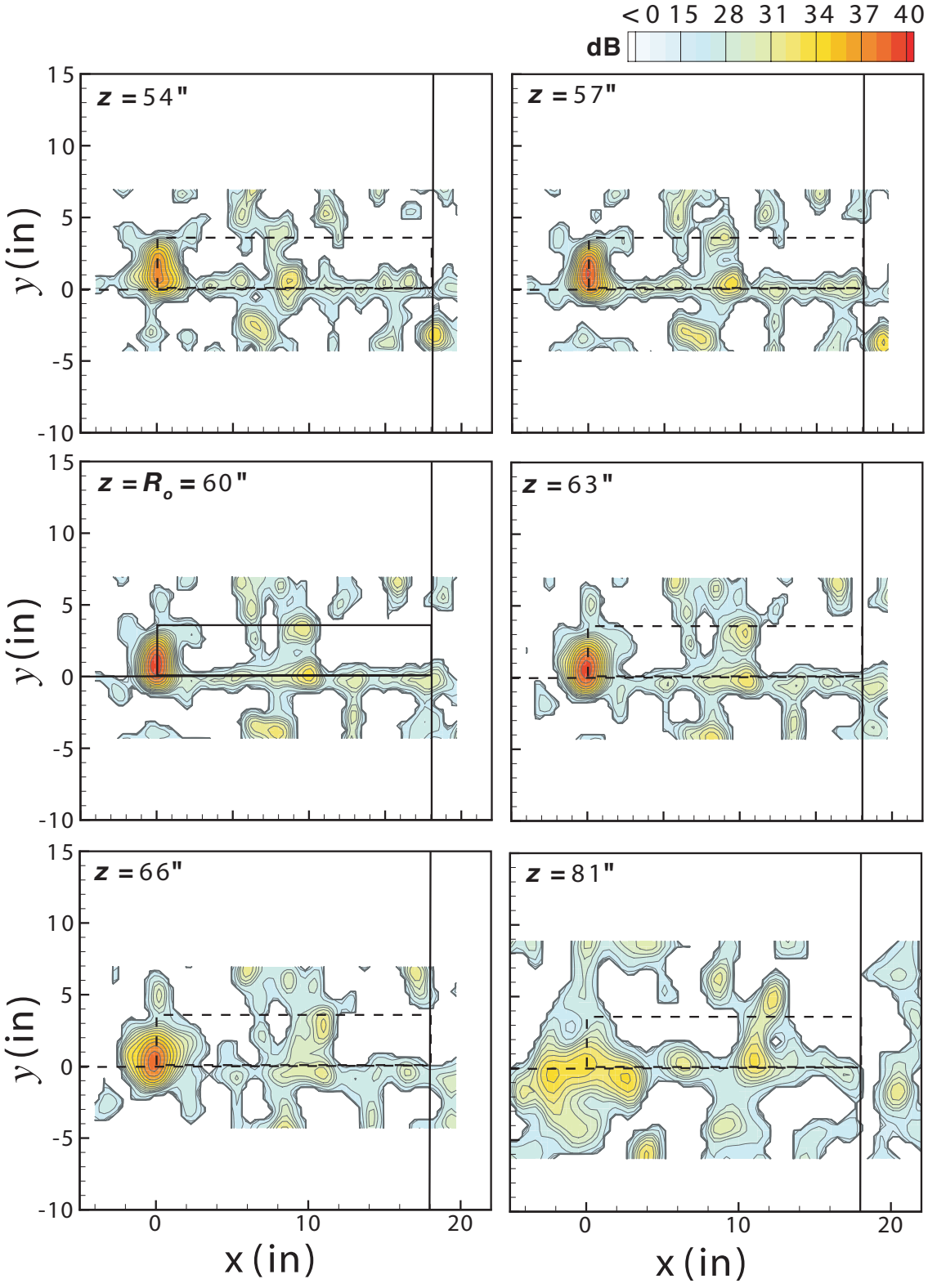

Figure 20. 3D beamforming output for flap noise test. DR processing with $f_{1/3} = 20kHz$. $\Delta x = 0.25$". Five stacked scan planes and one distant background scan plane.

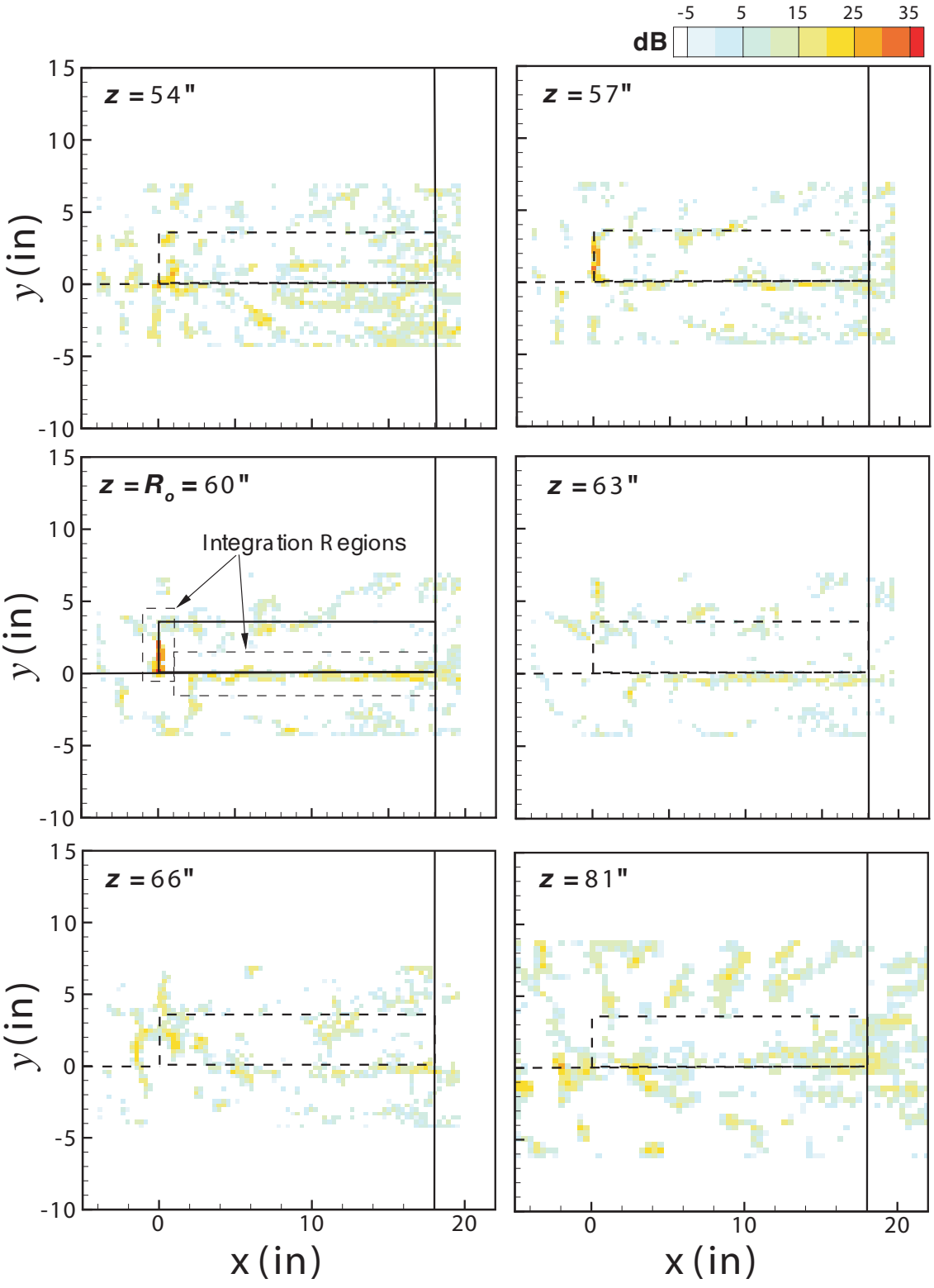

Figure 21. 3D DAMAS results corresponding to Fig. 20.

VT Landing Gear Test. An aeroacoustic noise test[6] was conducted for a 26%-scale, high-fidelity Boeing 777 main landing gear (LG) model in the Stability Wind Tunnel at the Virginia Polytechnic Institute and State University (Virginia Tech, VT). The model was previously tested at VT[7] and at NASA Ames Research Center[8]. A portion of the VT measurements was conducted by NASA LaRC with the primary purpose of demonstrating the use of an array using Micro-Electro-Mechanical System (MEMS) sensors[6].

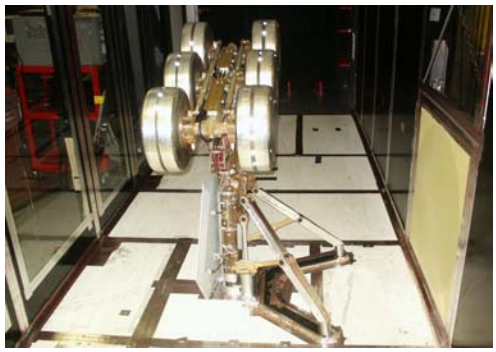

Figure 21. MEMS array in side mounted with 26% scale 777 landing gear test set-up in the Virginia Tech Stability Wind Tunnel.

The 128 MEMS microphone array is shown mounted in the sidewall of the 6 by 6 foot test section mounted beside the LG in Fig. 21. A ceiling mount was also employed in the test. The array pattern is shown in Fig. 7. The array is recessed from the tunnel wall by 1" and is covered by a tautly drawn Kevlar material to maintain wall integrity and to prevent boundary layer turbulence from producing pressure fluctuations directly over the microphones. This reduced noise floor levels substantially. Because of the edge blockage about the array cut-out, the outer microphone ring is not employed making the array effectively 32" in diameter with an active xx microphones. Figure 22 shows a top-view of the LG image and the side-wall mounted MEMS array with locations indicated for scanning plane cuts used in the 3D beamforming and DAMAS calculations. As was done for the preceding flap calculations, to keep the number of grid points down to approximately 20,000, a reduced number of grid planes in the source region is used. But in contrast no distant grid planes are used. With the array at z = -1", the stacked planes are at z = 19", 24", 29", 33.5", 38", and 43".

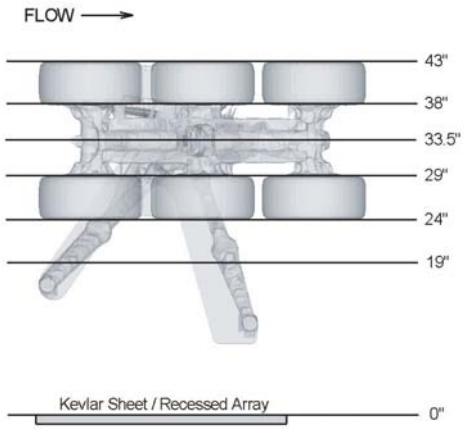

Figure 22. Stacked scan planes in 3D Beamforming and DAMAS for landing gear of Fig. 21

Figures 23 and 24 show beamforming and DAMAS results from the side-wall mounted array for the LG with the wheel truck angle at 13° and the tunnel Mach number at M = 0.17. The one-third octave presentations are for $f_{1/3}$= 6.3 kHz. With the array being relatively large and close to the distributed LG source region, the parameters cited as important for 3D DAMAS calculations are defined in a mean sense. Strictly speaking, because sources exist over each plane, each can be regarded as defining a R_0 position. However, upon choosing as a reference source distance $R_0 \approx$ 1"+ 33.5", one has $R_0/D \approx 1.08$. Using preceding equations, one has $R_1 \approx$ 26.9", $R_2 \approx$ 46.8", $B_l \approx$ 20", $B_l' \approx$ 15.2", so the resolution is calculated as $\lambda \approx$ 3". Nominally $B_{Wo} \approx$ 2.3", so with Δx = .85", one has $\Delta x / B_{Wo} \approx .37$ (which is outside of γ / B_{Wo} range between .05 and .2). For the W= 50" and H= 50", chosen to cover the spatial range of the LG. The planes are large with respect to the lateral beamwidth, $W/B_{Wo} = C_{Wo} \approx 22$. The space between planes in the stack is Δz= 4.5" and 5", which exceeds the reference resolution λ given above. (No accounting is attempted for any effective increases in the value for B_l and subsequently λ that may relate to the turbulent boundary layer scattering effects that was found present for the flap noise test application.) The present grid is seen to be a significant compromise that exceeds or are on the border of acceptable values of parameters important to 3D DAMAS application. For this reason, the application is considered preliminary.

In Fig. 23, the beamform results for the different cut planes show a substantial concentrated noise region toward the strut braces. In the planes farther from the array, sources more toward the wheel truck become apparent. Note that the steering vectors, Eq. (2), for the microphones accounts for shear layer refraction at the wall/tunnel flow interface at z = 0 and the mean tunnel flow convection speed. The effects of the Kevlar sheet at the shear layer interface has not been taken into account in the steering vectors.

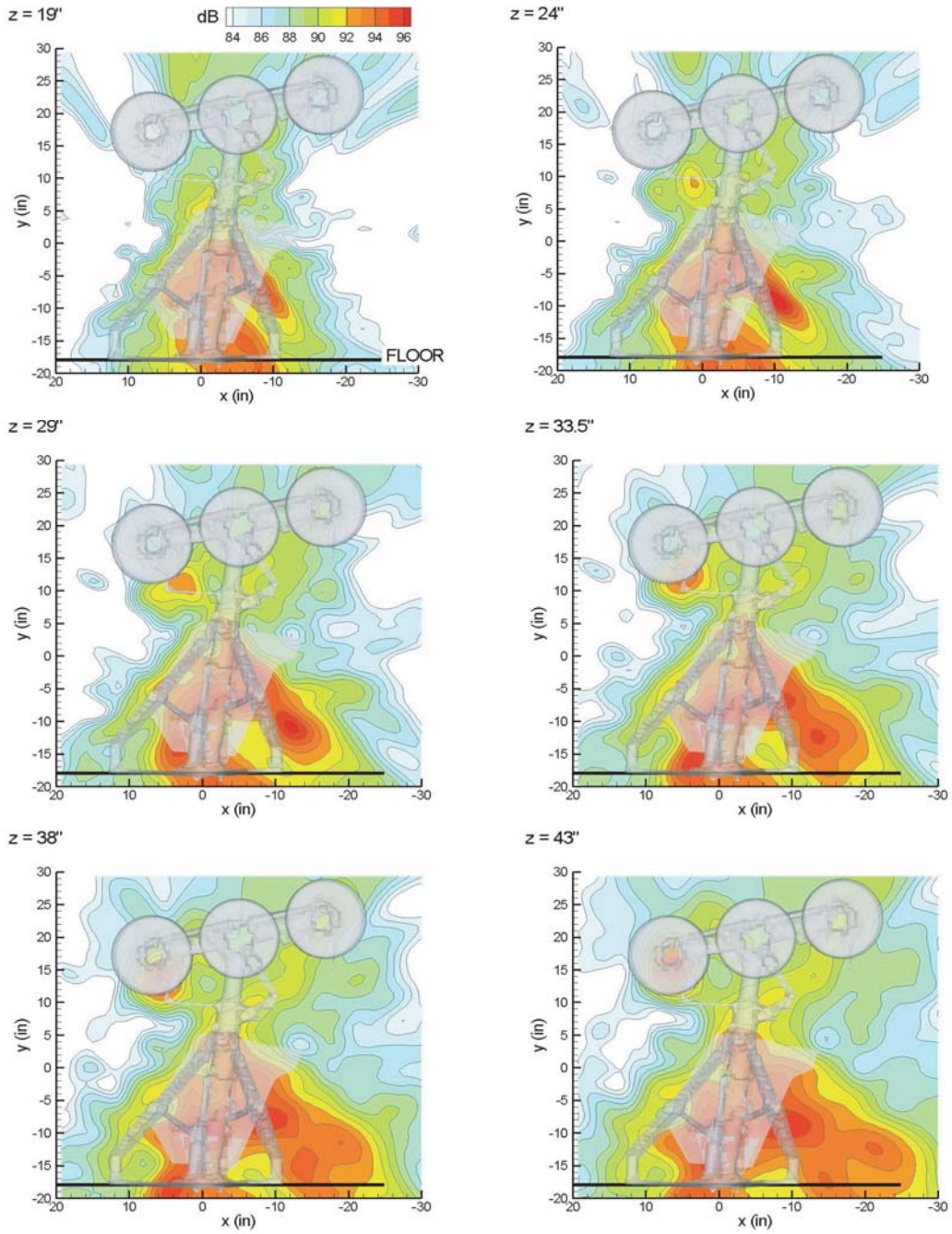

Figure 23. 3D Beamforming results for side-mount MEMS array over 6 planes about the LG.

The corresponding DAMAS results in Fig. 24 separate and quantify sources between the chosen planes. The first plane from the array at z = 19" cuts through the outer portion of the strut braces. Noise contributions from the braces appear to stand out, although there are sources assigned to the upper and center part of the plane that have to be regarded as being extraneously positioned. The next plane is at z = 24", just in front of the wheels that are nearest the array. The plane cuts about midway through the strut brace assemblies, which seem to show strong distributed noise sources. For the third plane at z = 29", just behind the near wheels, there appear to be contributions from the upper part of the strut braces and cross members. For the center plane for the truck assembly at z = 33.5", and over planes just in front of and behind the far wheels at z = 38" and 43", there seems to be contributions from the front brake and cable harness areas about the wheel truck, as well as the door panel and its mounts on the other side of the

strut. It is remembered that DAMAS assigns dB level to sources with respect to the level perceived by the array. Therefore, for a source that is farther from the array to give the same level, as one that is closer, it would have a higher "source strength".

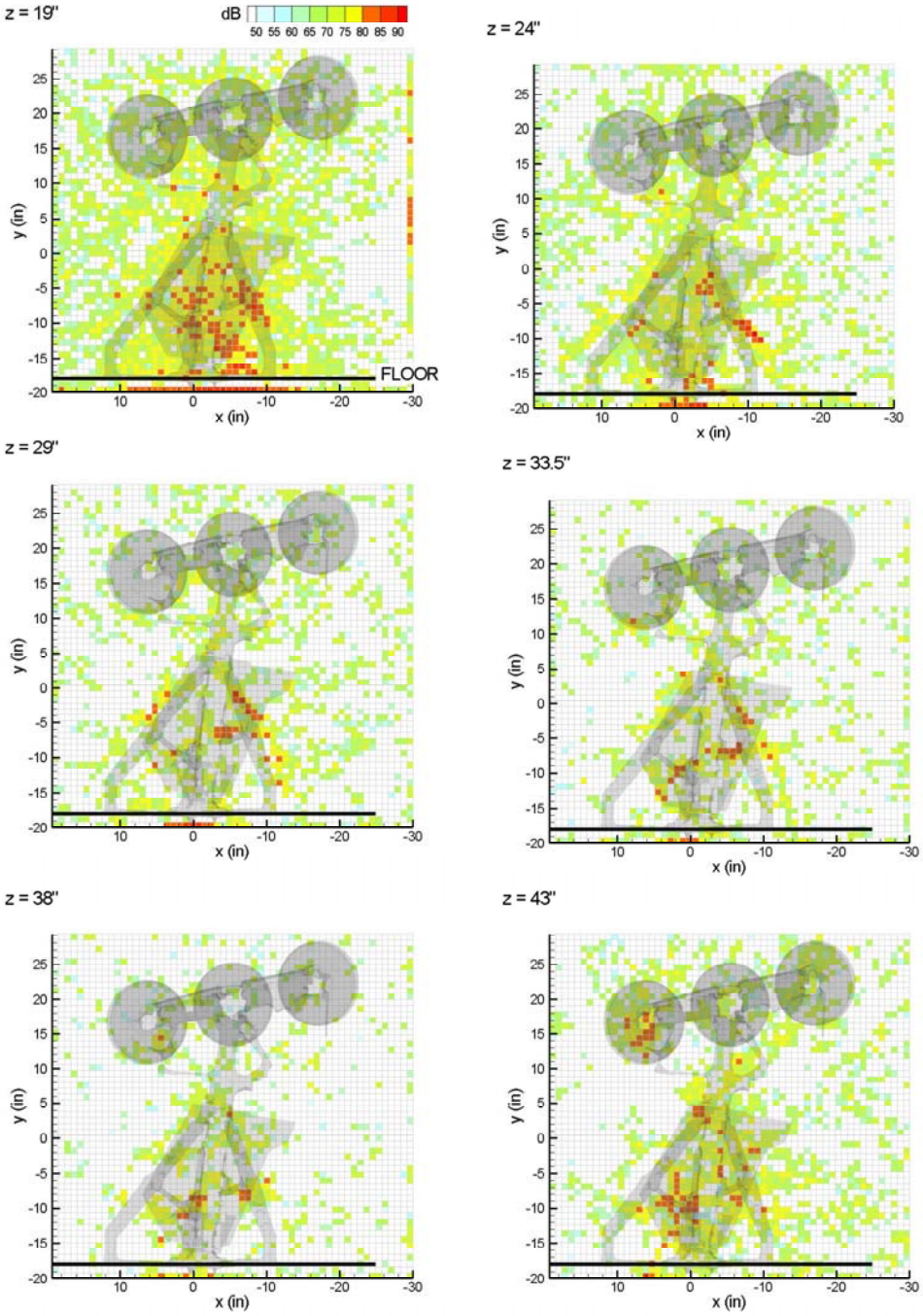

Figure 24. 3D DAMAS results for side-mount MEMS array corresponding to Fig. 23.

With respect to Fig. 24, there are sources distributed over the borders of the scanning planes, particularly along the bottom below the floor reference lines on the first and last scanning planes. This effect is discussed in Ref. 1, where it is mentioned that DAMAS apparently assigns "energy" or sources to borders when beamforming results suggest all sources are not within the defined scanning plane(s). Note that the floor region is a strong source of reflection that is not included in the particular grid planes chosen. Not included, also, is distant scanning planes

which potentially could be used to account for reflected / reverberant noise due to the tunnel walls. Some preliminary calculations indicated it would be counterproductive or wasted for this array and source orientation, which showed no identifiable strong reflection directions except for the afore-mentioned floor. The present application of Fig. 24 is not considered optimal.

V. Conclusions

Previously, beamforming and DAMAS post processing was dealt with only for single 2D scanning planes. The present paper examines the techniques for 3D applications. The basic beamforming ability of arrays, with regard to size and design, to focus longitudinally and laterally is evaluated as a function of frequency and distance. For all practical designs and measurement situations considered, it was found that the longitudinal beamwidths B_l are large compared to their lateral beamwidths B_{Wo}. At 10 kHz, for a particular 34" diameter array at 60" from a source, B_l ≈27.5" and B_{Wo}≈2.6", so B_l/ B_{Wo}≈ 10.6. This restricts one's ability to attain good resolution in all directions. Still, array design does have an impact on measurement practicality. It was found that some existing arrays rate relatively well in this regard. Formulations are developed to predict attainable beamforming spatial resolution as a function of design. These were validated and incorporated in an evaluation of the ability of DAMAS to extract the source location and strength from beamformed results. It was found that the attainable spatial resolution λ (containing all source energy within 1 dB) was about 15% of the longitudinal beamwidth B_l. This percentage is about the same for lateral resolution, for 2D and 3D, with respect to lateral beamwidth B_{Wo}. An experimental calibration, which did not involve tunnel flow, validated this but found some additional spatial smearing to attain λ of about 20% of the theoretical B_l.

Experimental data from two different wind tunnel tests were examined in this study. A flap noise test was used to evaluate 3D DAMAS for multiple sources of different type distributions. The model was in an open-jet tunnel flow and the array was placed outside. It was found that the attainable resolution λ was less that than ideal at about 25% of the calculated B_l for a strong localized flap edge source. For a more broadly distributed flap cove noise, λ was about 40% of B_l. This is believed to be the result of an effective beamforming related increase in B_l due to the presence of turbulence, and subsequent noise ray path scattering, in the open-jet shear layer. This is viewed as problem that limits somewhat the potential routine utility of 3D beamforming and subsequent DAMAS application. The effect would also be found in closed wall wind tunnels where arrays are mounted a sidewall with an associated turbulent boundary layer.

The other experimental application is that of a landing gear in a closed wall windtunnel. In this case the array is relatively large and close with respect to distributed landing gear noise sources. This is not considered an optimum application, as there were some compromises made with regard to grid coverage and DAMAS application parameters. Still, the DAMAS results did successfully demonstrate the ability to separate and quantify sources over regions of the landing gear model.

References

1. T.F. Brooks and W.M. Humphreys, Jr., A Deconvolution Approach for the Mapping of Acoustic Sources (DAMAS) Determined from Phases Microphone Arrays, 10th AIAA/CEAS Aeroacoustics Conference, Manchester, UK, May 10-12, 2004, AIAA-2004-2954.

2. W.M. Humphreys, Jr., T.F. Brooks, W.W. Hunter, Jr., and K.R. Meadows, Design and Use of Microphone Directional Arrays for Aeroacoustic Measurements, 36th Aerospace Sciences Meeting, Reno, NV, January 12-15, 1998, AIAA-98-0471.

3. Marcolini, M.A., and Brooks, T.F., "Rotor Noise Measurement Using a Directional Microphone Array," *Journal of the American Helicopter Society*, pp. 11–22, 1992.

4. T.F. Brooks and W.M. Humphreys, Jr., Effect of Directional Array Size on the Measurement of Airframe Noise Components, 5th AIAA/CEAS Aeroacoustics Conference, Bellevue, WA, May 10-12, 1999, AIAA-99-1958.

5. J.S. Bendat and A.G. Piersol, *Engineering Applications of Correlation and Spectral Analysis*, John Wiley & Sons, New York, N. Y., 1980.

6. W.M. Humphreys, Jr., Q.A. Shams, S. S. Graves, B. S. Sealey, S. M. Bartram, Application of MEMS Microphone Array Technology to Airframe Noise Measurements, 11th AIAA/CEAS Aeroacoustics Conference, Monterey, CA, May 23-25, 2005, AIAA-2005-xxxx.

7. P.A. Ravetta, R.A. Burdisso, and W.F. Ng, "Wind Tunnel Aeroacoustic Measurements of a 26%-scale 777 Main Landing Gear Model", 10th AIAA/CEAS Aeroacoustics Conference, Manchester, UK, May 10-12, 2004, AIAA 2004-2885.

8. S.M. Jaegar, N.J. Burnside, P.T. Soderman, W.C. Horne, and K.D. James, "Microphone Array Assessment of an Isolated, 26%-Scale, High-Fidelity Landing Gear", 8th AIAA/CEAS Aeroacoustics Conference, Breckenridge, CO, 2002, AIAA Paper 2002-2410.